Article

Extreme air–sea turbulent fluxes during tropical cyclone Barijat observed by a newly designed drifting buoy

Xuehan Xie [a,b,*], Zexun Wei [c], Bin Wang [d,*], Zhaohui Chen [e,f], Marilena Oltmanns [g], Xiangzhou Song [a,b]

[a] Key Laboratory of Marine Hazards Forecasting, Ministry of Natural Resources, Hohai University, Nanjing 210098, China
[b] College of Oceanography, Hohai University, Nanjing 210098, China
[c] First Institute of Oceanography, Ministry of Natural Resources, Qingdao 266061, China
[d] National Ocean Technology Center, Ministry of Natural Resources, Tianjin 300112, China
[e] Physical Oceanography Laboratory, Ocean University of China, Qingdao 266100, China
[f] Qingdao National Laboratory for Marine Science and Technology, Qingdao 266237, China
[g] National Oceanography Centre, Southampton SO14 3ZH, United Kingdom

ARTICLE INFO

ABSTRACT

Using *in situ* observations collected by a drifting air–sea interface buoy (DrIB) in the northern South China Sea from August 30 to September 13, 2018, the extreme air–sea turbulent fluxes that occurred from September 8 to 13 during tropical cyclone (TC) Barijat were investigated. The most striking features were substantial increases in momentum and heat fluxes, with maximum increases of 10.8 m s^{-1} in the wind speed (WS), 0.73 N m^{-2} in the wind stress, 68.1 W m^{-2} in the sensible heat fluxes (SH) and 258.8 W m^{-2} in the latent heat fluxes (LH). The maximum WS, wind stress, SH and LH values amounted to 15.3 m s^{-1}, 0.8 N m^{-2}, 70.9 W m^{-2} and 329.9 W m^{-2}, respectively. Using these new DrIB observations, the performance of two state-of-the-art, high-resolution reanalysis products, ERA5 and MERRA2, was assessed. The consistency of the observed values with ERA5 was slightly better than with MERRA2, reflected in higher correlations but both products underestimated the WS during TC conditions. In calm weather conditions, the turbulent heat fluxes were overestimated, because they simulated a too dry and cold atmospheric state, enhancing the air–sea differences in temperature and humidity. Considering that an accurate representation of the air–sea turbulent and momentum fluxes is essential for understanding and predicting ocean and atmospheric variability, our findings indicate that more high-quality temperature and relative humidity observations are required to evaluate and improve existing reanalysis products.

1. Introduction

Tropical cyclones (TCs), traditionally called typhoons in the Pacific, are catastrophic weather processes for human society in the Earth system. The cyclonic circulation that occurs in tropical and subtropical oceans features low pressure, significantly enhanced winds and precipitation [1–4]. During the passage of a cyclone, the combined effects of decreased solar radiation and enhanced air–sea turbulent heat fluxes (THFs) cool the upper ocean, resulting in a cold wake at the surface [5–8]. Studying THFs during cyclone passages is meaningful for the prediction of TC paths and intensities [9,10]. Currently, the ability to forecast TC intensity is still an ongoing research area because TC intensity changes are not only related to complex atmospheric vortex dynamics and thermodynamics but are also closely related to air–sea interactions [7,10–14]. For example, TC Nargis (2008) rapidly intensified from a

weak category-1 storm to an intense category-4 storm within one day in the Bay of Bengal, inducing a death toll exceeding 130,000 and other tremendous losses [15]. The developmental mechanism of this TC resulted from a nearly 300% increase in THFs, with warm ocean anomalies supporting such rapid intensification [10]. Thus, understanding how THFs vary during TCs is vital for improving forecasting abilities.

However, due to the limitations of air–sea observation platforms under extreme weather conditions, TC observations have remained a challenging problem for many years [16–18]. *In situ* buoy observations are the major approach by which air–sea physical parameters are obtained and fluxes are estimated during TCs. However, TC passages are rare and often require extensive buoy resources, causing high demands regarding the durability and cost of buoys. Therefore, the long-term lack of *in situ* direct observations recorded during TCs has seriously hindered research on air–sea interactions and operational work, such as TC fore-
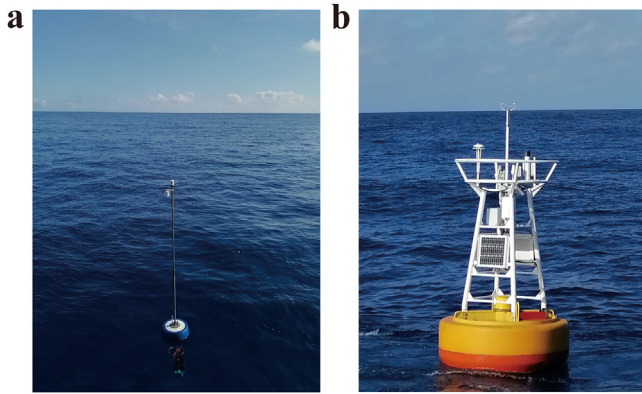

Fig. 1. Prototypes of a DrIB (a) and Bailong buoy (b) following deployment on a recent cruise in the South China Sea in the early summer of 2021.

Fig. 2. Trajectories of TC Barijat (the orange curve with triangles) and the DrIB (red dots) during the storm. The dates (month. day. hour) are incorporated along with the trajectory. The colored background indicates the SLP (unit: hPa) obtained from ERA5 at 0:00 on September 11, 2018, with a contour interval of 1 hPa. The thicker white contours highlight the center of TC Barijat. The land is drawn in grey.

casting [7,18]. In the Indo-Pacific region and the northwestern Pacific Ocean, moreover, a complete set of observed air–sea parameters, which is essential for estimating the air–sea net heat flux (Q_{net}), is largely lacking, impeding the analysis of Q_{net} anomalies that occur during TCs. Thus, additional efforts are required to quantitatively collect Q_{net} data in order to obtain a better understanding of the air–sea interactions that occur during the passage of TCs. A recent study examined three TCs in the southeastern Indian Ocean that passed by the Bailong buoy (located at 16.9°S, 115.2°E [19]). All three TCs were associated with active Madden–Julian Oscillation (MJO [20–24]) events. The most striking finding at the Bailong mooring site during these TCs was the extensively suppressed diurnal Q_{net} cycle, with a mean daytime (nighttime) reduction of 470 (131) W m^{-2}, a maximum decrease of 695 W m^{-2} at approximately noon and an extreme drop of 800 W m^{-2} during TC Riley [25]. Motivated by the results of this earlier study, the objective of the present analysis is to characterize the air–sea fluxes during TC events in more detail, using *in situ* observations, to advance our understanding of the associated THF anomalies and assess their representation in reanalysis models.

In view of the limitations of existing TC observation methods, a new observational concept has been developed: new drifting air–sea interface buoys (DrIBs). DrIBs combine the advantages of moored buoys and surface drifters (Fig. 1a). In contrast to traditional surface drifters, each DrIB is equipped with a 3-m-long mast made of aviation aluminum, an ultrasonic weather station (with a 3.0-m height) for measuring the wind speed (WS), wind direction and sea level pressure (SLP), and a temperature-humidity meter (with a 2.8-m height) for measuring the surface air temperature (SAT) and relative humidity (RH), thus forming a meteorological measurement module. In addition to the mast, the upper unit of each buoy also includes a hemispherical float with a maximum diameter of 0.54 m, a thermometer for measuring the sea surface temperature (SST) affixed to the bottom of the buoy, and a wave transducer for measuring wave-related parameters located inside the buoy, forming a hydrological measurement module. The recorded observations are transmitted in real time through the Beidou or Iridium satellite back to the data center after online quality control is performed. The float affixed to each buoy can also provide sufficient buoyancy for the DrIB such that it does not need to be fixed in a certain position with a mooring rope and can instead freely drift to measure the abundant essential ocean variables (EOVs) and essential climate variables (ECVs) on the air–sea interface. Compared to traditional air–sea buoys, such as Bailong buoys (Fig. 1b), the major advantage of DrIBs are their low costs and simple deployment and maintenance. Currently, more than 45 DrIBs have been deployed and maintained in regions such as the Western Pacific and the Indian Ocean after passing laboratory and near-shore tests. Comparisons performed between the air–sea variables measured with the Kuroshio Extension Observatory (KEO) buoy and research vessels indicate that the DrIBs are capable of measuring key pa-
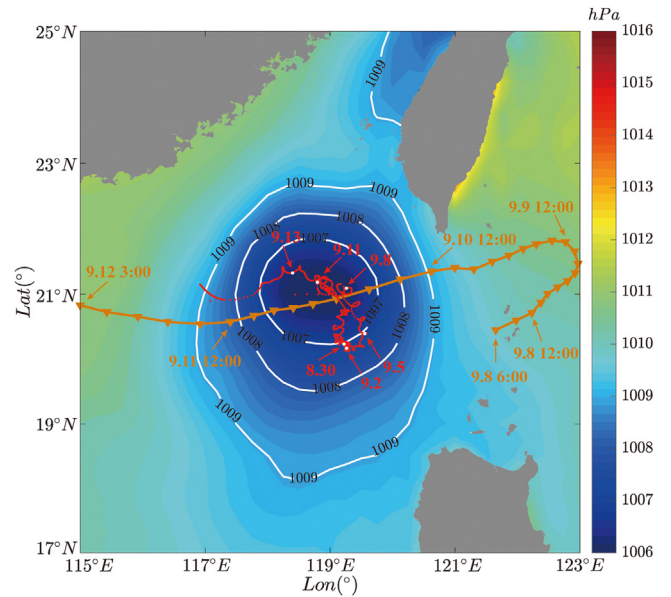
rameters at the air–sea interface with satisfactory quality. Thus, DrIBs provide an efficient and economical way to broadly observe air–sea turbulent fluxes during TCs at higher frequencies compared to moored buoys.

This study has two purposes. First, the observational ability of the new conceptual instrument, the DrIB, is evaluated during TC Barijat (2018) in the north South China Sea. This region is an area of significant TC genesis, with TC intensities reaching the tropical storm (TS) level or stronger [26–29]. Second, two state-of-the-art atmospheric reanalysis products are assessed against these observations to specifically evaluate their performance during the extreme air–sea turbulent flux variations that occurred in the South China Sea. The remainder of this paper is organized as follows: Section 2 introduces the DrIB observations, reanalysis flux products and data-processing methods such as the utilized bulk formulas; Section 3 investigates the physical mechanisms of high-resolution (hourly) turbulent flux anomalies during TC Barijat (2018) associated with marine boundary layer stability; in Section 4, the observed air–sea turbulent fluxes are used to evaluate the turbulent flux anomaly estimates based on two representative high-resolution reanalysis products; and finally, the summary and discussion are given in Section 5.

2. Data and methods

2.1. Data description

2.1.1. Buoy observations

Several DrIBs were deployed in advance of the TC season in the northern South China Sea in 2018 to observe the variable air–sea conditions during TCs. According to the records of the National Meteorological Center, TC Barijat intensified from a tropical depression (TD) to a TS at 8:00 on September 11. It passed by the DrIB from September 8 to 13, 2018 (Fig. 2). To compare air–sea flux anomalies associated with the extreme TC states relative to those associated with calm weather conditions, we obtained the air–sea parameters from the DrIB over the period from August 17 to September 15. We subsequently classified the observations from August 30 to September 7 as representa-

Table 1
Information about the air–sea variables observed by a DrIB in 2018.

Parameter	Manufacturer and sensor	Resolution	Range	Accuracy	Frequency (Hz)	Nominal depth or height[a] (m)
Sea level pressure	AirMar, 220WX	0.1 mbar	850∼1050 hPa	±1 hPa	1	3
Surface air temperature	NOTC, SHT16-1	0.1°C	-20∼50°C	±0.25°C	1	2.8
Relative humidity	NOTC, SHT16-1	1% RH	0∼100% RH	±3% RH	1	2.8
Wind direction	AirMar, 220WX	0.1°	0∼360°	±10°	1	3
Wind speed	AirMar, 220WX	0.1 m/s	0∼40 m/s	< 5% RMS	1	3
Sea surface temperature	NOTC, MT15	0.001°C	-2∼35°C	±0.005°C	1	-0.2

[a] Nominal depth or height represents the observational height (unit: m; a negative number represents the depth underneath the sea surface) above the sea surface.

tive of calm weather conditions, while the observations recorded from September 8 to 13 were considered to reflect TC states. The DrIB samples parameters at 1 Hz and averages them over two minutes. For the purpose of this study, hourly values are used. The detailed observational information of the air–sea variables used in this study (buoy number: 300234065559040) is listed in Table 1.

The International Best Track Archive for Climate Stewardship (IBTrACS) is a comprehensive global dataset developed by the National Climatic Data Center (NCDC) of the National Oceanic and Atmospheric Administration (NOAA) in cooperation with the World Data Center for Meteorology (Asheville). This dataset comprises the number, best tracks and characteristics of TCs reported globally and provides these data for public use [30]. IBTrACS provides TC information every three hours, and the temporal range of the TC Barijat data spans from 6:00 on September 8 to 18:00 on September 13, 2018. According to the data provided by the National Meteorological Center, the cyclone was in a TD state from 8:00 on September 10 to 5:00 on September 11; a TS state from 8:00 on September 11 to 4:00 on September 13; and in a strong TS state from 5:00 on September 13 to 9:00 on September 13. Then, the TC made landfall in Guangdong, China. The TC intensity weakened rapidly after landing, passing through two TS and TD stages.

2.1.2. Newly released atmospheric reanalysis datasets

Based on the Goddard Earth Observing System Model (GEOS) version 5.12.4, the Modern-Era Retrospective analysis for Research and Applications Version 2 (MERRA2 [31]) dataset was produced by the National Aeronautics and Space Administration (NASA) Global Modeling and Assimilation Office (GMAO) and covers the time period from 1980 to the present. This new reanalysis product incorporates further advances and replaces MERRA [32]. The European Centre for Medium-Range Weather Forecasts (ECMWF) Reanalysis version 5 (ERA5) dataset provides hourly estimates of a large number of atmospheric, ocean-wave and land-surface variables from 1979 to present [33]. ERA5 replaced the ERA-Interim reanalysis [34]. Both ERA5 and MERRA2 are based on advanced data assimilation systems and combine advanced models and observations from all over the world into global reanalysis datasets. MERRA2 provides hourly oceanic sensible heat (SH) and latent heat (LH) data as well as the associated SST, SAT, specific humidity and WS variables. ERA5, in addition to the above factors, provides richer variables such as the SLP and dew point temperature. The THFs provided by both reanalysis products were estimated based on the Louis algorithm [35]. ERA5 and MERRA2 output hourly air–sea variables, which is consistent with the temporal resolution of the DrIB, but the spatial resolutions of these reanalysis products are 0.25° × 0.25° and 0.625° (longitude) × 0.5° (latitude), respectively. The reanalysis products often have complex temporal properties, including instantaneous and time-averaged parameters.

2.2. Air–sea turbulent flux calculation method: bulk formulas

Using the DrIB observations, air–sea turbulent fluxes were calculated based on bulk formulas, namely, the Coupled Ocean Atmosphere Response Experiment (COARE) 3.5 algorithm [36–41]:

$$\tau = \rho C_D |u_z|^2 \tag{1}$$

$$Q_{SH} = \rho C_p C_H |u_z| (\Delta T) \tag{2}$$

$$Q_{LH} = \rho L_e C_E |u_z| (\Delta q) \tag{3}$$

where τ is the wind stress, Q_{SH} and Q_{LH} are the sensible heat flux and latent heat flux, respectively, ρ is the air density, u_z is the horizontal WS vector at height Z, C_p is the specific heat capacity of air, L_e is the latent heat flux of evaporation, C_D is the drag coefficient, C_H and C_E represent the turbulent exchange coefficients of SH and LH, respectively, and ΔT and Δq represent the air–sea temperature difference and air–sea humidity difference, respectively. Given that sea surface currents cannot be observed by the DrIB, only the absolute WS (u_z) with respect to the Earth is considered in the bulk formulas assuming that the influence of surface currents (SFCs) is less than that of surface winds. The effects of SFCs on the air–sea turbulent flux estimates were assessed in another study based on buoy observations [42].

2.3. Boundary layer stability (z/L) and Monin–Obukhov length (L)

Next, the physical mechanism affecting the hourly turbulent flux anomalies was investigated by computing the boundary layer stability (BLS). The BLS is traditionally determined using the Monin–Obukhov stability parameter z/L, where z represents the height of the turbulent transfer coefficient and L represents the Obukhov length scale estimated based on the COARE 3.5 algorithm. The Obukhov length scale indicates the ratio of Reynolds stress work to buoyancy work and is calculated as follows [43–45]:

$$L = \frac{u_*^2}{\kappa \frac{g}{\bar{T}} T_*}, T_* = -\frac{\overline{w'T'}}{u_*} \tag{4}$$

where the prime notation represents fluctuating values; u_* is the friction velocity; $\kappa \approx 0.4$ is the von Kármán constant; g is the gravitational acceleration constant; $\bar{T}$ is the average temperature of the boundary layer; and $\overline{w'T'}$ is the Reynolds stress term, which can be expressed by multiplying the spatial derivative of T by the turbulent exchange coefficient, with T and w representing the temperature and vertical motion, respectively. Classical theory holds that unstable, near-neutral and stable BLSs are defined by $z/L < -0.4$, $-0.4 < z/L < 0.1$, and $z/L > 0.1$, respectively [46].

3. Physical mechanism of turbulent flux anomalies in terms of BLSs

3.1. Analytical results obtained for DrIB observations

Taking advantage of the air–sea physical variable measurements, the bulk formulas (Eqs. 1–3) were used to estimate the air–sea turbulent fluxes, including the wind stress, SH and LH fluxes. Fig. 3 shows the time series of air–sea variables during the observational period. Table 2 shows the air–sea variable anomalies between calm weather and extreme conditions in terms of their change rates. An evident cold wake with a magnitude of 0.4 °C was found from September 8 to 13
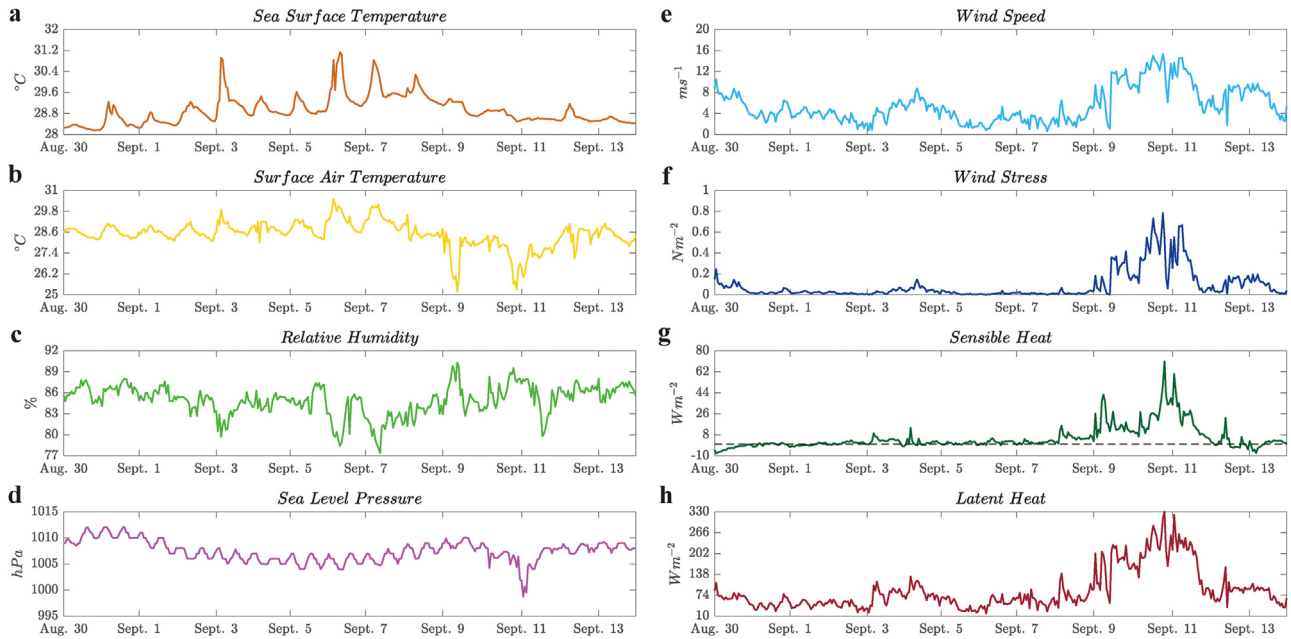
Fig. 3. Time series of observed air–sea variables. (a) SST (unit:˚C), (b) SAT (unit:˚C), (c) RH (unit: %), (d) SLP (unit: hPa), (e) WS (unit: m s^{-1}), (f) wind stress (unit: N m^{-2}), (g) SH (unit: W m^{-2}), and (h) LH (unit: W m^{-2}).

Table 2
Mean air–sea variable values and increase rates.

	SST (˚C)	SAT (˚C)	RH (%)	SLP (hPa)	WS (m s^{-1})	Wind stress (N m^{-2})	SH (W m^{-2})	LH (W m^{-2})
Calm weather conditions[a]	29.0	28.7	84.5	1007.6	4.5	0.05	2.9	71.0
Extreme cyclone conditions[a]	28.6	27.9	86.0	1006.9	9.2	0.23	12.9	148.9
Increase rate[b]	-1.4%	-2.7%	2%	-0.1%	103%	360%	348%	110%

[a]Calm weather conditions and extreme cyclone conditions are defined as the average air–sea conditions during the calm weather and extreme cyclone states, respectively. [b]Increase rate represents the mean values under extreme cyclone conditions relative to calm weather conditions.

during the passage of TC Barijat, consistent with the findings of previous studies [8]. Meanwhile, the SAT dropped by 0.8 ˚C as a result of the low heat capacity of the atmosphere, causing a higher air–sea temperature difference and a potential increase in SH. The RH slightly increased during the passage of TC Barijat from 84.5% to 86.0%. The SLP dropped to as low as 1006.9 hPa, reflecting the passage of the TC, with the WS reaching values of 15.3 m s^{-1}, the wind stress amounting to 0.8 N m^{-2}, and the SH and LH values climbing to 70.9 W m^{-2} and 329.9 W m^{-2}, respectively. The maximum increases in these variables were 10.8 m s^{-1} for the WS, 0.73 N m^{-2} for the wind stress, and 68.1 W m^{-2} and 258.8 W m^{-2} for the SH and LH, respectively. These results indicate a significant enhancement of the air–sea momentum and heat fluxes during the passage of TC Barijat, as observed by new DrIB, and confirm the resilience of this platform to extreme weather conditions.

3.2. Effects of wind and temperature (humidity) anomalies on the hourly turbulent flux anomalies measured under a near-neutral BLS

The variations in THFs are closely related to the BLS, corresponding to the work done by the buoyancy and wind processes. Using Eq. 4 and the COARE 3.5 algorithm, the boundary layer was found to have near-neutral and unstable conditions. Near-neutral BLS conditions were dominant in the warm season due to the relatively small air–sea temperature differences, with occasionally unstable BLS conditions (Fig. 4). Notably, during the transit of TC Barijat from September 8 to 13, the BLS mainly reflected near-neutral conditions. The same finding was reported in our previous study [25]. According to traditional notions, the Monin–Obukhov length is large under near-neutral
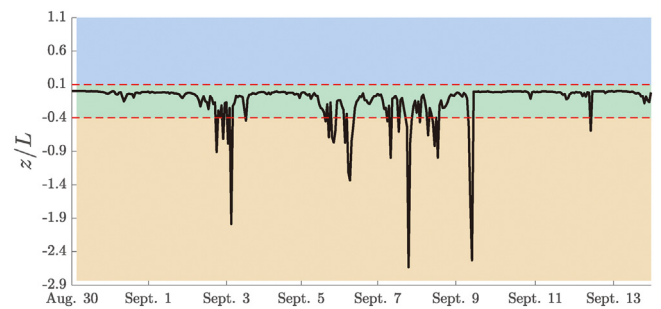

Fig. 4. The boundary layer stability (BLS) parameter z/L estimated based on Eq. 4. The delineations between unstable conditions (z/L < -0.4; yellow shading) and near-neutral conditions ($-0.4 < z/L < 0.1$; green shading) and between near-neutral conditions and stable conditions $z/L > 0.1$ (blue shading) are separated by two red dotted lines, $z/L = -0.4$ and $z/L = 0.1$, respectively.

BLS and infinite as the parameter $z/L \approx 0$. This indicates the dominant role of the wind effect in the marine boundary layer during TC Barijat. On September 9, an unstable BLS was due to a sudden increase in the air–sea temperature difference due to the different heat capacities of the ocean and atmosphere. However, the BLS quickly returned to a near-neutral state, consistent with the surrounding atmospheric environment.

Using the hourly wind stress, SH, LH and related air–sea physical variable estimates, the influence of the wind effect (term B in Eqs. 5–7) and thermal effect (term C in Eqs. 6,7) on the hourly turbulent flux anomalies under near-neutral conditions was investigated. Assuming
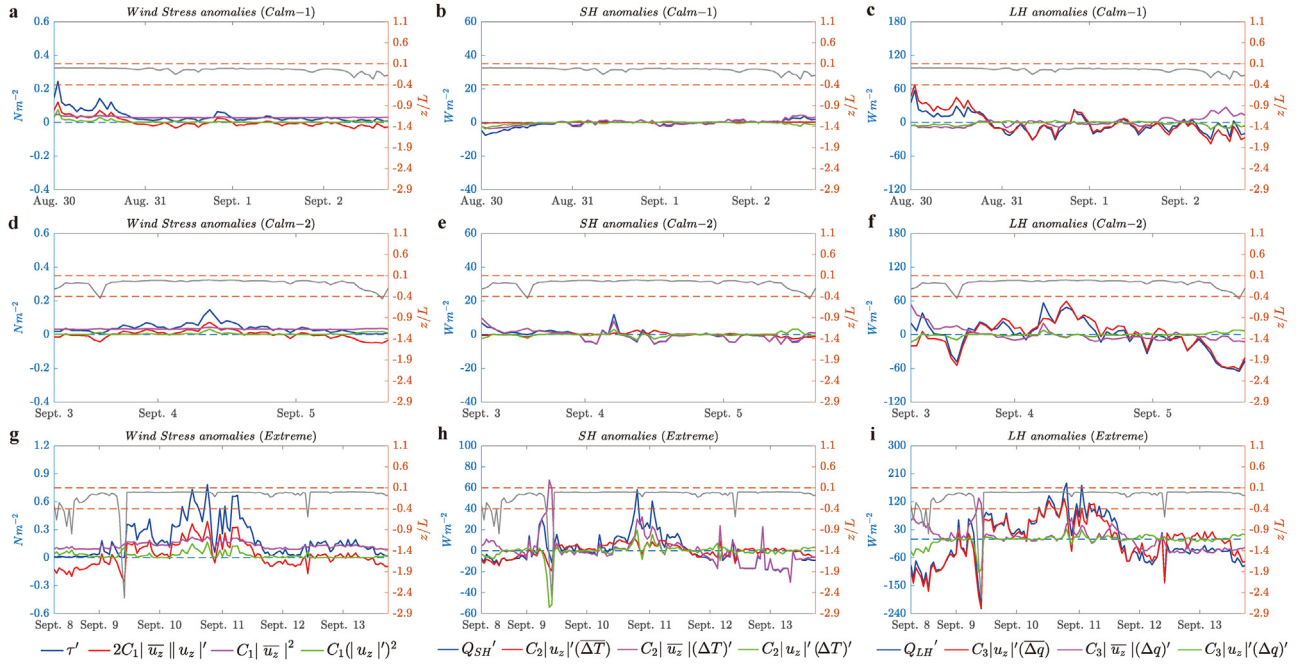
Fig. 5. Time series of the hourly anomalies of each term (blue *y*-axis) under a near-neutral BLS in Eqs. 5–7. (a) wind stress anomalies (τ' in Eq. 5, blue, term A), with term B denoting the wind stress anomalies caused by wind anomalies ($2C_1|\overline{u_z}||u_z|'$ in Eq. 5, red), term C representing the average WS term varying with C_1 ($C_1|\overline{u_z}|^2$ in Eq. 5, magenta), and term D denoting the nonlinear term ($C_1(|u_z|')^2$ in Eq. 5, green) during the first stage of calm weather before TC Barijat passage; (b) is similar to (a), but terms A∼D represent SH anomalies, wind anomalies, air–sea temperature difference anomalies and nonlinear terms, respectively; and (c) values corresponding to those shown in (b) but for hourly LH anomalies and associated terms. The middle (d∼f) and bottom (g∼i) panels are the same as the upper panels but for the second stage of calm weather conditions and extreme cyclone conditions, respectively. The gray line is the boundary layer stability parameter z/L as a reference (orange *y*-axis).

that the coefficients $\rho C_D = C_1$, $\rho C_p C_H = C_2$ and $\rho L_e C_E = C_3$ from Eqs. 1∼3, the hourly turbulent flux anomalies in Eqs. 5∼7 were obtained as follows:

$$\underbrace{\tau'}_{Term\ A} = C_1\left[\underbrace{2|\overline{u_z}||u_z|'}_{Term\ B} + \underbrace{|\overline{u_z}|^2}_{Term\ C} + \underbrace{(|u_z|')^2}_{Term\ D}\right] \quad (5)$$

$$\underbrace{Q'_{SH}}_{Term\ A} = C_2\left[\underbrace{|u_z|'(\overline{\Delta T})}_{Term\ B} + \underbrace{|\overline{u_z}|(\Delta T)'}_{Term\ C} + \underbrace{|u_z|'(\Delta T)'}_{Term\ D}\right] \quad (6)$$

$$\underbrace{Q'_{LH}}_{Term\ A} = C_3\left[\underbrace{|u_z|'(\overline{\Delta q})}_{Term\ B} + \underbrace{|\overline{u_z}|(\Delta q)'}_{Term\ C} + \underbrace{|u_z|'(\Delta q)'}_{Term\ D}\right] \quad (7)$$

where the l.h.s. (left-hand side) term represents the hourly air–sea turbulent flux anomalies, as denoted by term A; terms B and D in the r.h.s. (right-hand side) represent the wind effect and nonlinear effect terms, respectively; and term C in the r.h.s. represents the average WS in Eq. 5 and thermal effect in Eqs. 6,7. An overbar indicates the average of the relevant variable during continuous and constant near-neutral BLS. An apostrophe (') indicates an anomaly in the corresponding variable relative to its average state. The other symbols in Eqs. 5–7 are the same as those in Eqs. 1–3.

Fig. 5 shows the physical mechanisms of hourly turbulent flux anomalies during calm weather and extreme cyclone conditions under a near-neutral BLS. By comparing the correlation coefficient (*r*) values (Table S1), it is found that the hourly wind anomalies play central roles in both wind stress and LH anomalies, while hourly SH anomalies are mainly controlled by wind anomalies and air–sea temperature difference anomalies. Hourly wind stress anomalies are dominated by hourly wind anomalies, with *r* values of 0.95–0.98, regardless of calm

weather or extreme cyclone conditions. The influence of the nonlinear terms on wind stress anomalies cannot be neglected, with *r* values of 0.86, 0.34 and 0.65 during the two-stage calm weather and extreme cyclone conditions, respectively. Air–sea temperature difference anomalies have the most significant influence on hourly SH anomalies, with *r* even reaching 0.91 to 0.94 in calm weather and 0.65 in extreme cyclone. Hourly wind anomalies play a secondary role in SH anomalies, and its influence is slightly larger during the first stage of calm weather (*r* = 0.65) than during extreme cyclone conditions (*r* = 0.54). The nonlinear terms also have an influence on hourly SH anomalies, with *r* values of 0.48 and 0.29 during the first stage of calm weather and extreme weather, respectively. The influence of wind anomalies on LH anomalies is the most significant under all weather conditions (*r* = 0.92–0.95) and is only slightly lower than the influence of wind anomalies on wind stress anomalies. Hourly air–sea humidity difference anomalies have very little effect on LH anomalies during extreme cyclones (*r* = 0.07), while the influence of nonlinear terms on LH anomalies is larger (*r* = 0.52). In addition, the root mean square error (RMSE) and standard deviation (STD) values were calculated to further corroborate the conclusions obtained by comparing *r* values (Table S1).

We note that sudden increases in air–sea temperature and humidity differences led to a few unstable BLS conditions dominated by buoyancy fluxes under extreme conditions. For example, there was a peculiar signal on September 9. The results indicate that wind conditions can directly impact turbulent fluxes in terms of Eqs. 5–7. However, wind can also drive dynamic movements in the upper ocean, promote the formation of air–sea temperature differences, indirectly lead to heat exchange and catalyze phase changes. Here, we calculated only the local effect of wind anomalies in contributing to the hourly THF anomalies without considering their indirect effects, which are associated with general basin-scale ocean circulation and beyond the scope of the current study.
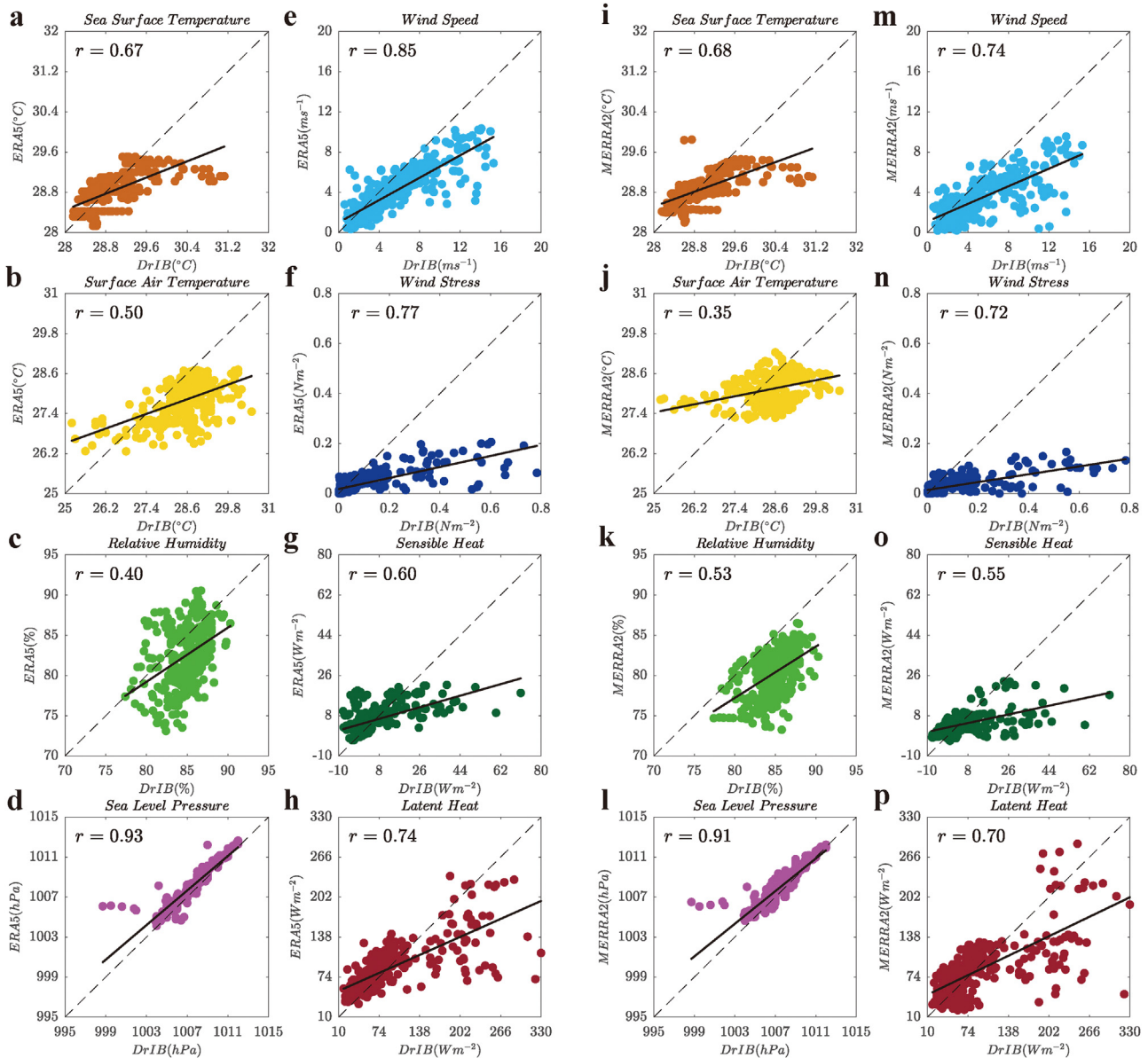
Fig. 6. Scatter plots measuring the correlation degrees of air–sea variables between the DrIB measurements (*x*-axis) and reanalysis products (*y*-axis). The left panels denote ERA5, and the right panels denote MERRA2: (a) SST (unit:°C), (b) SAT (unit:°C), (c) RH (unit: %), (d) SLP (unit: hPa), (e) WS (unit: m s^{-1}), (f) wind stress (unit: N m^{-2}), (g) SH (unit: W m^{-2}), and (h) LH (unit: W m^{-2}). Panels (i) – (p) reflect the same values as (a) – (h). The linear regression is represented by solid black lines, and the correlation coefficient (*r*) values at a 95% confidence level are incorporated into the panels. It should be noted that the WS heights of ERA5, MERRA2 and DrIB have been unified to 3 m based on the wind profiles [47].

4. Assessment of ERA5 and MERRA2 reanalyses against the DrIB observations

The WS, temperature and turbulent flux terms recorded by DrIB were used to evaluate the recently released high-resolution atmospheric reanalysis products ERA5 and MERRA2. The TC signals captured in the reanalysis are shown in Fig. S1 and Table S2. Fig. 6 shows the derived scatter plots of the DrIB observations and reanalysis products in terms of air–sea variables, revealing two main characteristics. First, all variables recorded during TC Barijat in the reanalysis products show lower linear regressions compared to the DrIB observations. Second, except for the SST and RH, the other variables in ERA5 indicate slightly higher correlations (*r* values) with the DrIB observations compared to those in MERRA2. The reanalyzed turbulent fluxes in this section were recalculated based on COARE 3.5 to investigate the errors caused by differences in parameterization schemes (Figs. S2, S3). The SST mainly reflected

weak correlations under calm weather conditions, showing an *r* of 0.67 (0.68) with the ERA5 (MERRA2) product. As the diurnal SST cycle is not resolved in the reanalyses, compared to the observations, the reanalysis time series are characterized by a lack of extreme values before TC passages (Fig. S1). TC Barijat tended to cause a low-temperature surface environment with less diurnal variation. The SAT in the reanalysis generally showed colder signals, but some exceptions were obtained under the TC. The *r* of SAT is 0.50 (0.35) for ERA5 (MERRA2). The cause of this difference may be related to the more severe heat loss at the air–sea interface, or it may have resulted from a height difference of the DrIB measurements (2.8 m) compared to the reanalysis output (2 m). In most cases, the reanalysis simulated a drier environment, especially MERRA2, although ERA5 (*r* = 0.40) was less capable of simulating RH than MERRA2 was (*r* = 0.53). The accuracy of SST, SAT, WS and RH is strongly influenced by the spatial and temporal resolution. In particular, the time series obtained from the DrIB observations exhibited the most
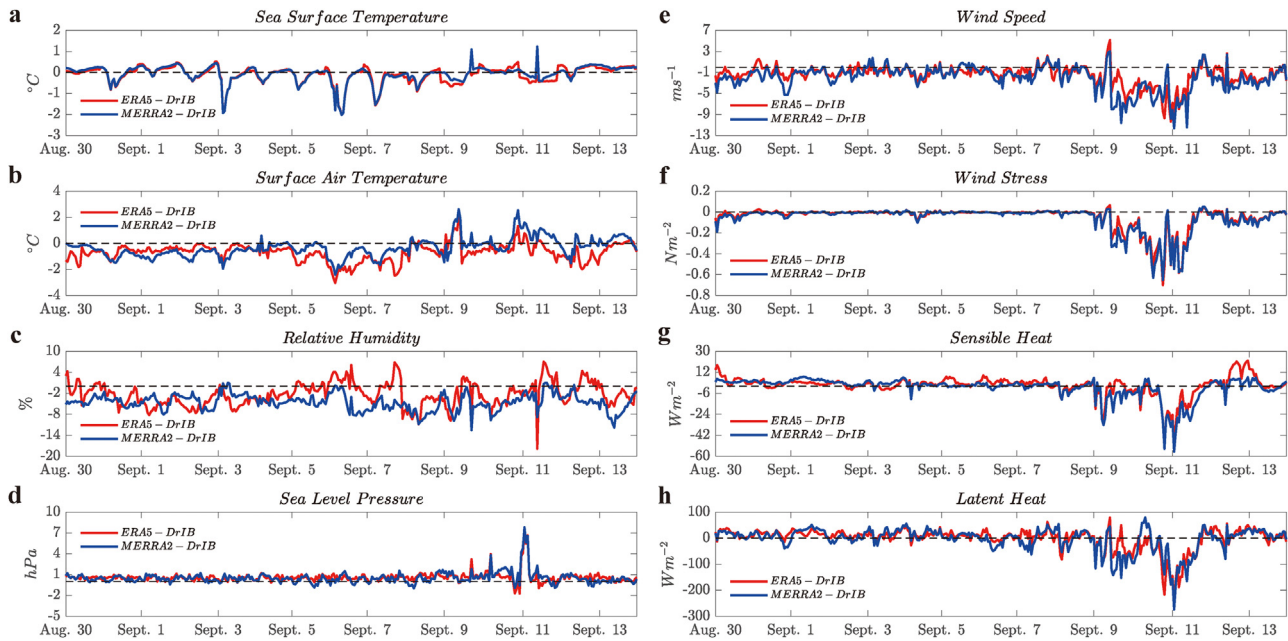
Fig. 7. Time series of the differences between the reanalysis products and DrIB measurements. (a) SST (unit:°C), (b) SAT (unit:°C), (c) RH (unit: %), (d) SLP (unit: hPa), (e) WS (unit: m s^{-1}), (f) wind stress (unit: N m^{-2}), (g) SH (unit: W m^{-2}), and (h) LH (unit: W m^{-2}). The differences reflect the reanalysis product values minus the DrIB-measured values.

dramatic fluctuations, while ERA5 and MERRA2 simulate smoother evolutions. Among the two, the MERRA2 time series is smoother than that of ERA5, as shown in Fig. S1. Considering the importance of small-scale processes for the intensification of the TCs, we attribute the lower WS and wind stress estimates of the reanalyses to their lower resolution. The correlation of WS was the best among the variables, with an r value of 0.85 (0.74) for ERA5 (MERRA2), and that of wind stress was the second best, with an r value of 0.77 (0.72) for ERA5 (MERRA2). The height of the WS, obtained from the reanalyses matches that of the observations [47], and there is little difference between the reanalysis and recalculation results ($r = 0.99$). THF is similar to wind stress in terms of the reanalysis values being significantly lower that the observations for extreme signals. However, different parameterization schemes can also introduce biases in the THF estimation, in addition to the lower resolution (Fig. S3). Under calm conditions, the THF estimates in the reanalyses are higher, which is attributed to biases in the simulated temperature and humidity environment. To determine the exact cause, however, a more detailed analysis is needed. Lastly, the uncertainty in the individual terms on which the turbulent fluxes are based remains a large error source. The correlation of SH is weakly affected by the temperature, with an r value of 0.60 (0.55) for ERA5 (MERRA2). LH is dominated by the WS, the corresponding correlation is significantly better than that of SH, with an r value of 0.74 (0.70) for ERA5 (MERRA2). The results show a slightly weaker correlation for THF compared to wind stress due to the poor performance of the simulated temperature and humidity terms, while the WS data is comparatively more accurate.

Fig. 7 shows the time series of the differences between the reanalysis products and DrIB measurements, revealing two main features. First, the differences in air–sea variables between ERA5/MERRA2 and DrIB show similar variations during the observational period, indicating equivalent simulation abilities of the two reanalyses. Second, the meteorological variables reflected in the reanalysis during the TC passage were not accurately simulated, showing lower WS, SAT and turbulent flux values compared to the observed values. The largest discrepancy in the SST occurs during calm weather, with a bias magnitude of approximately 2°C. The mean deviation in ERA5 (MERRA2) was 0.16 (0.13)°C lower than that of DrIB during calm weather, while it was 0.02 (0.07)°C higher than that of DrIB during the TC passage. The SAT in the reanalysis typically

exhibits large deviations of 1~3°C below the observations and, occasionally, 1~2°C above the observations during extreme cyclones (the peaks in Fig. 7b). Combined with RH, this indicates the simulation of a colder and drier atmospheric state. For the WS and wind stress, the reanalysis estimates were lower than the DrIB measurements; the average differences between the ERA5 (MERRA2) values and DrIB measurements were 1.1 (1.6) m s^{-1} and 0.02 (0.03) N m^{-2} during calm weather, respectively, and 2.7 (3.4) m s^{-1} and 0.14 (0.16) N m^{-2} during the TC passage, respectively. As expected, the maximum deviations in the WS and wind stress occurred during the TC passage, at 10.3 (11.7) m s^{-1} and 0.70 (0.65) N m^{-2}, respectively. The development of higher spatial and temporal resolution WS data can further improve the simulation of wind terms during extreme cyclones. For SH and LH, the reanalysis estimates were lower than the observed values during the TC passage, with ERA5 (MERRA2) averages of 2.3 (7.5) W m^{-2} and 26.9 (23.1) W m^{-2}, respectively, but were higher during calm weather, with ERA5 (MERRA2) averages of 1.6 (0.9) W m^{-2} and 6.2 (1.9) W m^{-2}, respectively. Similar to the WS and wind stress, the largest deviations in SH and LH also occurred during the TC, with the ERA5 (MERRA2) values being lower than the DrIB measurements by 52.8 (56.1) W m^{-2} and 250.3 (274.4) W m^{-2}, respectively. The results suggest that reducing the uncertainty of THF estimates in extreme environments plays an important role in improving estimates of the global heat balance. This can be achieved by optimizing the parameterization methods used to estimate extreme THF and improving the fidelity of the simulated temperature and humidity at higher spatial and temporal resolutions.

In our evaluation, we found that compared to DrIB measurements, reanalyses tend to produce higher THF estimates during calm weather, despite the low valuation of WS in reanalyses. This indicates higher Δq and ΔT estimates in the reanalysis products, consistent with other studies on the influence of TCs Wallace, Riley and Veronica, based on recent buoy observations undertaken in the southeastern Indian Ocean [25]. A relatively dry and cold atmosphere may be simulated by reanalyses, causing them to output higher Δq and ΔT estimates. The validation results are shown in Fig. 8, where the ΔT values reflected by the reanalyses are generally higher than the DrIB measurements, with average discrepancies of approximately 0.6°C for ERA5 and 0.3°C for MERRA2, implying that the reanalyses simulate a colder atmosphere. The RH values
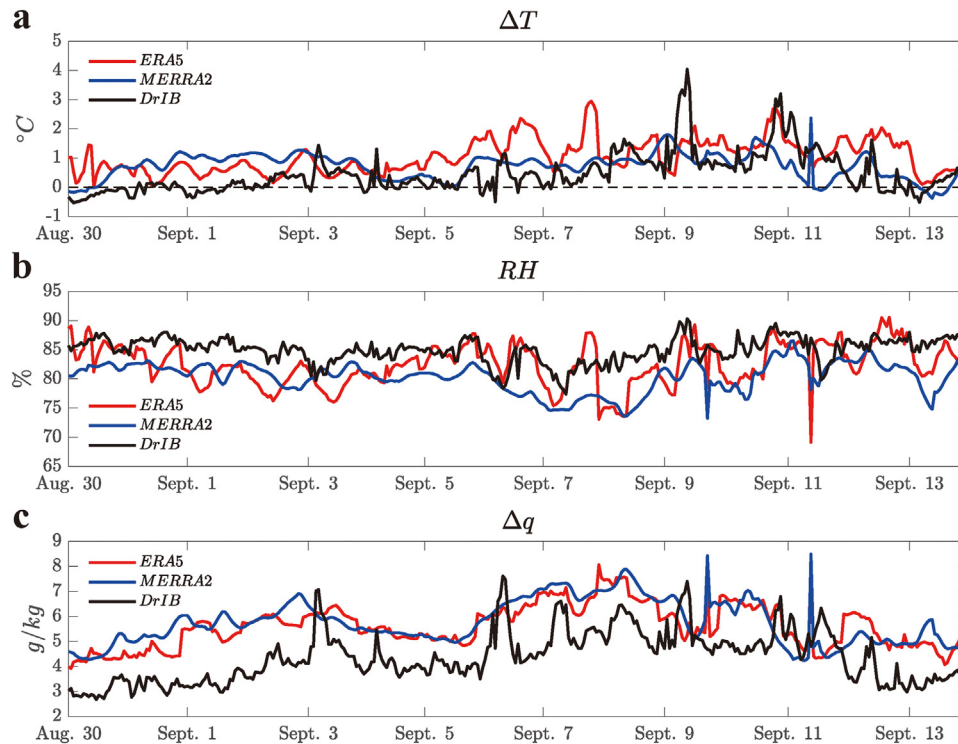
Fig. 8. Comparisons of the time series of air–sea variables derived from the ERA5/MERRA2 and DrIB measurements. (a) ΔT (unit:°C) reflects the difference between the SST and SAT, (b) RH (unit: %), and (c) Δq (unit: g/kg) reflects the difference in the saturation specific humidity between the SST and SAT. It should be noted that the calculation of RH for ERA5 and MERRA2 is based on the changing SLP (Fig. S1).

reflected in the reanalyses are artificially smaller than the DrIB observations, indicating relatively dry atmospheric conditions in the reanalysis simulations, with average differences of approximately 2.4% for ERA5 and 4.6% for MERRA2. The mean discrepancies in Δq were 1.2 g/kg for ERA5 and 1.4 g/kg for MERRA2. Higher Δq and ΔT values are typical for the reanalyses, regardless of calm weather or extreme cyclone conditions. However, the simulated THF in the reanalyses is still underestimated during extreme cyclones, due to the large bias in the WS during the TC passage (Fig. 7c).

5. Discussion and summary

A widespread limitation that has long restricted the development of TC intensity forecasting is the lack of accurate, reliable and cost-effective EOV and ECV observation methods under extreme weather conditions [18,19], resulting in few available high-precision, near-real-time *in situ* observations. The present study provides an *in situ* air–sea variable time series recorded by a newly developed DrIB from August 30 to September 13, 2018, in the northern South China Sea, during which TC Barijat passed. Based on bulk formulas, the extreme air–sea turbulent flux variations are obtained and analyzed, and the physical mechanisms affecting the hourly turbulent flux anomalies under a near-neutral BLS are explored. The observed air–sea variables and estimated turbulent fluxes are then used to evaluate the performance of the two newly released, state-of-the-art ERA5 and MERRA2 reanalysis products. The main findings are summarized as follows.

First, the maximum WS observed by the DrIB during TC Barijat reached 15.3 m s^{-1}, and the maximum wind stress, SH and LH values reached 0.8 N m^{-2}, 70.9 W m^{-2} and 329.9 W m^{-2}, respectively. The LH values were verified to be higher during the warm season, while the SH values were smaller, and the SST and SAT values were close. When TC Barijat passed, a near-neutral BLS was observed, while the air–sea turbulent fluxes increased significantly, with the maximum WS, wind stress, SH and LH increase values being 10.8 m s^{-1}, 0.73 N m^{-2}, 68.1

W m^{-2} and 258.8 W m^{-2}, respectively. The hourly wind stress (LH) anomalies during an extreme cyclone were dominated by wind anomalies and nonlinear terms, with r values of 0.98 (0.93) and 0.65 (0.52), respectively. Additionally, the hourly SH anomalies during an extreme cyclone were affected by the combined effects of thermal anomalies and wind anomalies, and the influence of nonlinear terms also could not be neglected, as these terms corresponded to r values of 0.65, 0.53 and 0.30, respectively. These factors were indirectly affected by the hourly wind anomalies. These analyses show that the high-resolution WS, SAT and SST observations and, in particular, the RH observations are vital when studying the extreme turbulent fluxes that occur during TCs.

Second, the observational ability of the DrIB under extreme weather conditions was examined in this study, and relevant air–sea variables were used to assess recently released atmospheric reanalyses. ERA5 showed a slightly better correlation than MERRA2. The WSs were simulated more accurately than the temperature and humidity in the reanalyses. For ERA5, the r values derived with the observations were 0.93 (SLP), 0.85 (WS), 0.77 (wind stress), 0.74 (LH), 0.67 (SST), 0.60 (SH), 0.50 (SAT) and 0.40 (RH); the corresponding r values obtained for MERRA2 were 0.91, 0.74, 0.72, 0.70, 0.68, 0.55, 0.35 and 0.53, respectively. The differences in the air–sea variables, simulated by the two reanalyses, relative to the DrIB measurements showed similar patterns. The reanalysis estimations of WS and wind stress were lower, especially during the TC. For SH and LH, the reanalysis estimates obtained during the TC were also lower, but those derived during calm weather were slightly higher due to the simulation of a relatively dry and cold atmosphere (lower RH) with higher Δq and ΔT estimates. This shows that ERA5 and MERRA2 still have difficulties to correctly simulate small- and medium-scale processes under extreme air-sea conditions and that higher resolutions or improved parametrization schemes are needed.

In conclusion, this study used *in situ* observations derived from a newly designed DrIB that can record scarcely measured extreme turbulent flux variations during TCs and revealed the physical mechanisms affecting high-resolution (hourly) turbulent flux anomalies.

These observations provide a valuable scientific basis for evaluating global reanalysis flux products such as ERA5 and MERRA2. It was found that ERA5 and MERRA2 do not accurately simulate the variations in extreme air–sea turbulent fluxes that occur during TCs. One of the main problems is the underestimation of the RH and WS and the overestimation of the temperature (humidity) difference reflected in these reanalysis products during TCs. More abundant and accurate *in situ* measurements of small- and medium-scale processes such as temperature and RH values are needed to verify reanalysis products.

The air–sea turbulent fluxes utilized in this study are estimated based on the COARE 3.5 algorithm, which differs from the Louis scheme used in the examined reanalysis products [35]. To avoid different parameterization methods used to estimate turbulent fluxes affecting the reliability of estimations, the air–sea turbulent fluxes in the reanalyses were recalculated based on the bulk formulas and checked in this paper (Figs. S2 and S3). The results show similar wind stress values between the original and recalculated values, but there are discrepancies in the THF. The use of different algorithms is reflects uncertainty around the optimal value for the turbulent exchange coefficient, which is the largest source of error in turbulent flux estimation [18]. We propose this as a key research direction to be explored in future studies.

In this paper, the observational capacity of the new conceptual instruments called DrIBs during TCs was effectively tested. The results motivate further studies to improve the performance of global reanalysis flux products and better understand the complex air–sea interactions that occur in sea areas where TCs frequently occur, such as the South China Sea [26–29]. However, DrIB observations and estimated air–sea turbulent fluxes are also accompanied by uncertainty. First, the height of the air–sea variables measured by DrIB affects the accuracy of THF estimation. For example, surface cooling due to increased heat losses can lead to a lower skin temperature than the temperature beneath the surface (SST measured at 0.2 m depth by DrIB), which is known as the cold skin effect [48]. Zhang et al. [49] determined that the South China Sea has a stronger cold skin effect than the tropical Pacific Ocean. Since existing cold skin models are based on the tropical Pacific Ocean (TAO/TRITON), skin temperatures in the South China Sea are underestimated. To circumvent this problem in future, temperatures at various depths provided by instruments such as DrIBs can be combined with shipboard skin temperature observations to obtain high-resolution *in situ* observations of the vertical temperature profile, which can help refine the cold skin model and thus improve the accuracy of THF estimation. Lastly, the motion of the 3-m DrIB platform on the sea surface during turbulent air–sea conditions can lead to uncertainties in the observations. Therefore, this paper is an empirical case that provides a reference for the study of extreme air–sea turbulent fluxes, and more *in situ* observations are required for verification. Mobile instruments, such as DrIBs, are a valuable resource in long-term air–sea observation networks that allow to better understand and predict air–sea interactions, assess their role in large-scale weather and climate variability and help constrain the ocean's energy budget.

Declaration of competing interest

The authors declare that they have no conflicts of interest in this work.

Acknowledgments

Supplementary materials

Supplementary material associated with this article can be found, in the online version, at doi:10.1016/j.fmre.2022.08.022.

References

[1] E. Palmen, On the formation and structure of tropical hurricanes, Geophysica 3 (1948) 26–38.
[2] A. Kasahara, Supplementary notes on the formation and the schematic structure of typhoons, J. Meteor. Soc. Japan 32 (2) (1954) 31–52.
[3] T.B. Stanford, P.G. Black, J. Haustein, et al., Ocean response to a hurricane. Part I: Observations, J. Phys. Oceanogr. 17 (11) (1987) 2065–2083.
[4] W.M. Gray, The formation of tropical cyclones, Meteorl. Atmos. Phys. 67 (1998) 37–69.
[5] E.L. Fisher, Hurricanes and the sea-surface temperature field, J. Meteor. 15 (3) (1958) 328–333.
[6] J.F. Price, Upper ocean response to a hurricane, J. Phys. Oceanogr. 11 (2) (1981) 153–175.
[7] K.A. Emanuel, Contribution of tropical cyclones to meridional heat transport by the oceans, J. Geophys. Res. 106 (D14) (2001) 14771–14781.
[8] E.A. D'Asaro, T.B. Sanford, P.P. Niiler, et al., Cold wake of Hurricane Frances, Geophys. Res. Lett. 34 (15) (2007) L15609.
[9] K.A. Emanuel, Sensitivity of tropical cyclones to surface exchange coefficients and a revised steady-state model incorporating eye dynamics, J. Atmos. Sci. 52 (22) (1995) 3969–3976.
[10] I.-I. Lin, C-H. Chen, I.-F. Pun, et al., Warm ocean anomaly, air sea Fluxes, and the rapid intensification of tropical cyclone, Geophys. Res. Lett. 36 (3) (2009) L03817.
[11] K.A. Emanuel, An air–sea interaction theory for tropical cyclones. Part I: Steady-state maintenance, J. Atmos. Sci. 43 (6) (1986) 585–605.
[12] K.A. Emanuel, Thermodynamic control of hurricane intensity, Nature 401 (1999) 665–669.
[13] M. Demaria, M. Mainelli, L.K. Shay, et al., Further improvements to the Statistical Hurricane Intensity Prediction Scheme (SHIPS), Weather Forecast. 20 (4) (2005) 531–543.
[14] E.A. D'Asaro, P. Black, L. Centurioni, et al., Typhoon-ocean interaction in the western North Pacific: Part 1, Oceanography 24 (4) (2011) 24–31.
[15] P.J. Webster, Myanmar's deadly daffodil, Nat. Geosci. 1 (2008) 488–490.
[16] S. Landwehr, N. O'Sullivan, B. Ward, Direct flux measurements from mobile platforms at sea: Motion and airflow distortion corrections revisited, J. Atmos. Ocean. Technol. 32 (6) (2015) 1163–1178.
[17] L.R. Centurioni, J. Turton, R. Lumpkin, et al., Global in situ observations of essential climate and ocean variables at the air–sea interface, Front. Mar. Sci. 6 (2019) 419.
[18] M.F. Cronin, C.L. Gentemann, J. Edson, et al., Air–sea fluxes with a focus on heat and momentum, Front. Mar. Sci. 6 (2019) 403.
[19] H.P. Freitag, C. Ning, P.L. Berk, et al., ATLAS, T-Flex, Bailong meteorological sensor comparison test report, NOAA Tech. Memo. OAR PMEL 148 (2016) 31pp.
[20] R.A. Madden, P.R. Julian, Detection of a 40-50 day oscillation in the zonal wind in the tropical Pacific, J. Atmos. Sci. 28 (5) (1971) 702–708.
[21] R.A. Madden, P.R. Julian, Description of global-scale circulation cells in the tropics with a 40-50 day period, J. Atmos. Sci. 29 (6) (1972) 1109–1123.
[22] H.H. Hendon, M.L. Salby, The life cycle of the Madden–Julian oscillation, J. Atmos. Sci. 51 (15) (1994) 2225–2237.
[23] C. Zhang, Madden–Julian oscillation, Rev. Geophys. 43 (2) (2005) RG2003.
[24] C.A. DeMott, N.P. Klingaman, S.J. Woolnough, Atmosphere-ocean coupled processes in the Madden–Julian Oscillation, Rev. Geophys. 53 (4) (2015) 1099–1154.
[25] X. Song, C. Ning, Y. Duan, et al., Observed extreme air–sea heat flux variations during three tropical cyclones in the tropical southeastern Indian Ocean, J. Climate 34 (9) (2021) 3683–3705.
[26] G.-H. Wang, J. Su, Y.-H. Ding, et al., Tropical cyclone genesis over the south China sea, J. Mar. Sys. 68 (3-4) (2007) 318–326.
[27] A.Z.-C. Goh, J.C.L. Chan, Interannual and interdecadal variations of tropical cyclone activity in the South China Sea, Int. J. Climatol. 30 (6) (2010) 827–843.
[28] R.C.Y. Li, W. Zhou, Interdecadal change in South China Sea tropical cyclone frequency in association with zonal sea surface temperature gradient, J. Climate 27 (14) (2014) 5468–5480.
[29] B. Xiang, X. Dong, Y. Li, Climate change trend and causes of tropical cyclones affecting the South China Sea during the past 50 years, Atmos. Oceanic Sci. Lett. 13 (4) (2020) 301–307.
[30] K.R. Knapp, M.C. Kruk, D.H. Levinson, et al., The International Best Track Archive for Climate Stewardship (IBTrACS), Bull. Amer. Meteor. Soc. 91 (3) (2010) 363–376.
[31] R. Gelaro, W. McCarty, M.J. Suárez, et al., The Modern-Era Retrospective Analysis for Research and Applications, version 2 (MERRA-2), J. Climate 30 (14) (2017) 5419–5454.
[32] M.M. Rienecker, M.J. Suárez, R. Gelaro, et al., MERRA: NASA's Modern-Era Retrospective Analysis for Research and Applications, J. Climate 24 (14) (2011) 3624–3648.
[33] H. Hersbach, B. Bell, P. Berrisford, et al., The ERA5 global reanalysis, Quart. J. Roy. Meteor. Soc. 146 (2020) 1999–2049.
[34] D.P. Dee, S.M. Uppala, A.J. Simmons, et al., The ERA-Interim reanalysis: Configuration and performance of the data assimilation system, Quart. J. Roy. Meteor. Soc. 137 (656) (2011) 553–597.
[35] J.F. Louis, A parametric model of vertical eddy fluxes in the atmosphere, Bound.-Layer Meteor. 17 (1979) 187–202.

[36] W.T. Liu, K.B. Katsaros, J.A. Businger, Bulk parameterization of air–sea exchanges of heat and water vapor including the molecular constraints at the interface, J. Atmos. Sci. 36 (9) (1979) 1722–1735.

[37] C.W. Fairall, E.F. Bradley, D.P. Rogers, et al., Bulk parameterization of air–sea fluxes for Tropical Ocean-Global Atmosphere Coupled-Ocean Atmosphere Response Experiment, J. Geophys. Res. 101 (C2) (1996) 3747–3764.

[38] C.W. Fairall, E.F. Bradley, J.E. Hare, et al., Bulk parameterization of air–sea fluxes: Updates and verification for the COARE algorithm, J. Climate 16 (4) (2003) 571–591.

[39] M.A. Brunke, C.W. Fairall, X. Zeng, et al., Which bulk aerodynamic algorithms are least problematic in computing ocean surface turbulent fluxes? J. Climate 16 (4) (2003) 619–635.

[40] L. Yu, Global air–sea fluxes of heat, fresh water, and momentum: Energy budget closure and unanswered questions, Annu. Rev. Mar. Sci. 11 (2019) 227–248.

[41] X. Song, The importance of including sea surface current when estimating air–sea turbulent heat fluxes and wind stress in the Gulf Stream region, J. Atmos. Oceanic. Technol. 38 (1) (2021) 119–138.

[42] X. Song, The importance of relative wind speed in estimating air–sea turbulent heat fluxes in bulk formulas: Examples in the Bohai Sea, J. Atmos. Oceanic Technol. 37 (4) (2020) 589–603.

[43] A.S. Monin, A.M. Obukhov, Basic regularity in turbulent mixing in the surface layer of the atmosphere, Tr. Geofiz. Inst. Akad. Nauk SSSR 24 (1954) 163–187.

[44] W.G. Large, S. Pond, Sensible and latent heat flux measurements over the ocean, J. Phys. Oceanogr. 12 (5) (1982) 464–482.

[45] T.V. Blanc, An error analysis of profile flux, stability, and roughness length measurements made in the marine atmospheric surface layer, Bound. Layer Meteorol. 26 (1983) 243–267.

[46] W.G. Large, S. Pond, Sensible and latent heat flux measurements over the ocean, J. Phys. Oceanogr. 12 (1982) 464–482.

[47] S.D. Smith, Coefficients for sea surface wind stress, heat flux and wind profiles as a function of wind speed and temperature, J. Geophys. Res. 93 (1988) 15467–15472.

[48] C.W. Fairall, E.F. Bradley, J.S. Godfrey, et al., Cool-skin and warm-layer effects on sea surface temperature, J. Geophys. Res. 101 (1996) 1295–1308.

[49] R. Zhang, F. Zhou, X. Wang, et al., Cool skin effect and its impact on the computation of the latent heat flux in the South China Sea, J. Geophys. Res. 126 (2021) e2020JC016498.

Xuehan Xie is a graduate student in physical oceanography at the College of Oceanography, Hohai University. She got her bachelor's degree in marine science from HHU. Her research interests focus on the upper ocean dynamics and air-sea interactions based on the newly developed *in situ* oceanic observations.

Bin Wang (BRID: 05356.00.97130) is a senior engineer working for the National Ocean Technology Center affiliated with the Ministry of Natural Resources. The drifting air-sea interface buoy developed by his team has been deployed in more than 80 sets of high-medium-low sea areas around the world, basically possessing the global ocean operational observation capabilities.